Synthesis of Realistic Simultaneous Positron Emission Tomography and Magnetic Resonance Imaging Data

Irene Polycarpou, Georgios Soultanidis, and Charalampos Tsoumpas, *Senior Member, IEEE*

Abstract— **The investigation of the performance of different positron emission tomography (PET) reconstruction and motion compensation methods requires accurate and realistic representation of the anatomy and motion trajectories as observed in real subjects during acquisitions. The generation of well-controlled clinical datasets is difficult due to the many different clinical protocols, scanner specifications, patient sizes, and physiological variations. Alternatively, computational phantoms can be used to generate large data sets for different disease states, providing a ground truth. Several studies use registration of dynamic images to derive voxel deformations to create moving computational phantoms. These phantoms together with simulation software generate raw data. This paper proposes a method for the synthesis of dynamic PET data using a fast analytic method. This is achieved by incorporating realistic models of respiratory motion into a numerical phantom to generate datasets with continuous and variable motion with magnetic resonance imaging (MRI)-derived motion modeling and high resolution MRI images. In this paper, data sets for two different clinical traces are presented, ^{18}F-FDG and ^{68}Ga-PSMA. This approach incorporates realistic models of respiratory motion to generate temporally and spatially correlated MRI and PET data sets, as those expected to be obtained from simultaneous PET–MRI acquisitions.**

Index Terms— **Computer simulation, molecular imaging, motion compensation, PET, phantoms.**

I. INTRODUCTION

POSITRON emission tomography (PET) is an advanced molecular imaging technique that offers insights on the molecular pathways of humans and animals in vivo. A positron-emitter, e.g. ^{18}F and ^{68}Ga, is used to radiolabel a molecule of interest, of which picomolar amounts can be traced in the patient during the scan. The imaging duration for one bed position is usually short, e.g. 3 *min*, though some protocols may last even longer than 60 *min* [1]. Inevitably

during PET scanning the patient breathes continuously and potentially exhibits other internal and external body movements which create artifacts, occasionally so strong that may render the acquisition obsolete [2]. The causes of such motion artifacts are not only attributable to the physical movement of the radiotracer and deformations [3]–[5] but also to the lung density variation during respiration [6]. Compensation of motion artifacts is feasible by [7], [8] carefully accounting for all related factors [9]–[11]. For example, the attenuation map is usually measured using a separate CT or MRI acquisition and requires to be free of motion and be co-registered with the PET images at all times [12], [13]. Motion compensation requires a realistic representation of physical movements for the evaluation of correction algorithms [14]. Various controlled parameters that may affect the correction methods need to be investigated, and therefore a substantial number of clinical datasets is required for more precise investigations. Parameters encompassing the clinical data such as respiratory and cardiac gating of dynamic images to derive the corresponding spatial deformations make the creation of a complete database difficult because they include intra-gate motion. Alternatively, synthetic data can be developed based on computational phantoms that represent the human anatomy [13]. This enables the creation of large datasets in various disease states which provide a ground truth, otherwise unavailable during clinical studies [15], [16].

Many phantoms have been traditionally developed from segmented high resolution anatomical images (e.g. CT or MRI) such as the widely used XCAT [17], which model the human thorax anatomy and simulate both cardiac and respiratory motion. Computational phantoms have been extensively used in numerous applications, such as the optimization of detection systems, the validation of reconstruction algorithms, the study of physical effects including photon attenuation, scatter and motion [18], [19].

To incorporate motion into numerical phantoms many studies use registration of dynamic images with sufficient temporal and spatial resolution (e.g. CT and MRI) that derive voxel deformations in order to warp a 3D numerical phantom [20]. For example, in the case of the XCAT phantom, respiratory and cardiac motion information have been derived from CT [17].

Numerical phantoms together with software packages are used to simulate a PET acquisition, generating raw data in the form of sinograms. The most commonly used method is based

on Monte Carlo simulations, such as the open source software GATE [21]. Monte Carlo simulations can model precisely the physical phenomena involved, but have the drawback of high computational demand. To compensate for these limitations, fast analytic methods have been developed, e.g. STIR [22], ASIM [23] or CASTOR [24] open source software packages.

A scheme for simulating realistic dynamic PET sinograms using real MRI acquisitions and analytic simulations based on STIR was developed by Tsoumpas *et al.* [20]. This approach is extended further in this study by incorporating realistic models of respiratory motion into numerical phantoms in order to generate datasets with continuous and variable motion, as expected to be obtained during real simultaneous PET-MRI acquisitions [25], [26]. To perform this, real respiratory signals derived from PET-CT images are combined with MRI-derived motion modelling and high resolution MRI images. In addition, this study enhances the realism of these simulations by incorporating changes in the lung attenuation values at different respiratory cycle positions which arise from the density changes in the lung as a result of motion; a phenomenon discussed in detail by Holman *et al.* [6]. Our paper provides a detailed description of the synthesis of realistic 4D numerical computational phantoms and associate PET data with motion for two clinically used radiotracers: ^{18}F-FDG and ^{68}Ga-PSMA.

II. METHODS

The synthesis of realistic anthropomorphic PET data with aperiodic motion requires several independent steps: (A) Segmented high resolution images from MRI for the generation of the PET and attenuation images; (B) A motion model which can provide the motion transformation vectors at any time point; (C) A respiratory signal from internal navigators or external surrogates; (D) Software synthesizing the 4D computational phantom (i.e. both PET and attenuation distributions) which subsequently can be either forward projected, as performed in our framework, or otherwise simulated with a Monte Carlo simulator. Each step is discussed below:

A. High Resolution 4D MRI Dataset

A 4D dynamic MRI dataset of the thorax was obtained on a 1.5 T Philips Achieva^{TM} scanner with a 32-channel coil using a T_1 weighted turbo field echo (TFE) sequence with repetition time equal to 3.3 ms and echo time equal to 0.9 ms and a flip angle of 10^0. The MRI dataset was reconstructed voxel dimensions of $1.5 \times 5 \times 1.5$ mm^3 (feet-head, right-left, anterior-posterior) and temporal resolution 0.7 s per time frame. An additional dedicated electrocardiograph (ECG) triggered cardiac MRI scan was performed to obtain details for myocardium motion in order to avoid any cardiac motion during the high resolution cardiac MRI acquisition as described by Tsoumpas *et al.* [20]. The dynamic 3D acquisition was applied with parallel imaging sensitivity encoding factor of 2 in anterior-posterior and 4 in right-left direction to speed up the acquisition and obtain the entire thorax within the $500 \times 450 \times 245$ mm^3 field of view. In total, 105 frames of 3D MRI images of the thorax were acquired for

the same volunteer. The first 35 images were acquired during a normal breathing mode, the next 35 during a fast breathing and the last 35 during deep breathing.

More accurate attenuation maps were developed through the inclusion of information for bone regions which were extracted using an MRI Ultrashort Time Echo (UTE) acquisition. Anatomical information was obtained from a respiratory-triggered UTE scan of the same volunteer used previously as described in [27]. For these UTE acquisition, two images were acquired with different echo times and with respiratory gating. The field of view was $400 \times 400 \times 400$ mm^3, with a resolution equal to $2 \times 2 \times 2$ mm^3 and with the times TR/TE$_1$ = 6.5/0.14 ms and TE$_2$ = 4.6 ms. A flip angle of 10° was also applied. The gating was achieved using a pencil-beam navigator which was manually positioned on the right hemidiaphragm. The scan duration was typically 10 to 30 min depending on the breathing pattern of the subject and the sufficiency of respiratory gating. The two resulting images were subtracted to create a third image, which exhibits increased cortical bone contrast.

B. MRI-Derived Motion Model

To create the MRI-derived motion model each of the 105 MRI images was registered to the separately acquired reference breath hold image using a hierarchical registration algorithm [28]. The reference breath hold image was at the end-expiratory state. The respiratory signal was measured using a virtual pencil beam navigator, manually placed at a middle point of the diaphragm along the feet-head direction. This navigator was manually placed on the dome of the right hemi-diaphragm and orientated along the feet-head direction in the first image of the series. For each control point and for each of the 105 MRI images the displacements in x, y, and z directions were calculated and plotted as functions of the head-foot diaphragm translation signal (i.e. surrogate signal). The direction of motion (i.e. inspiration/expiration) was also calculated.

A curve based on second order polynomial functions is fitted to the x, y, and z displacements as a function of surrogate values. This non-linear function allows for the estimation of non-linear motion [29]. Polynomial fitting is applied for inspiration and expiration phases separately, using the constraint that the curves of the inspiration and expiration phases come across at the extreme navigator positions as shown in Fig. 1. As a result, a model is defined by a three polynomial coefficients vector a. The three coefficients define the location of the control point (i, j, k), the coordinate direction (x, y or z) and the breathing phase, d (inspiration or expiration). The coefficient a is a $[3 \times 3 \times 2]$ set of $[N_x \times N_y \times N_z]$ volumes, where N_i are the number of control points on the B-spline grid in each direction i. Each voxel is a scalar that corresponds to the displacement of that voxel in the image being transformed. Therefore, there is one volume for (a) each order of γ, (b) all three directions, and (c) a separate set of coefficients for inspiration and expiration.

To apply the motion model, the x, y, z displacements for all control points are estimated based on a single input navigator
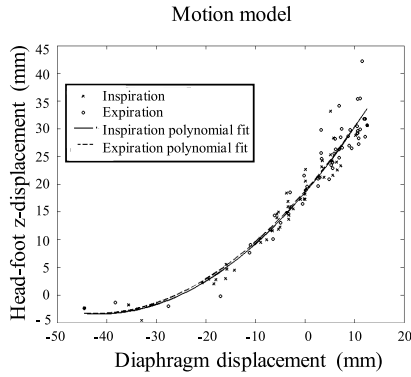
Fig. 1. Demonstration of the motion model. The control points are plotted separately for the inspiration and the expiration.

value, γ, and a breathing phase, d. The motion estimation at control point $\varphi_{i,j,k}$ is defined by the following equation [29]:

$$\hat{u}\left(\varphi_{i,j,k}\right) = \begin{pmatrix} \Psi(a_{i,j,k,x,d}, \gamma) \\ \Psi(a_{i,j,k,y,d}, \gamma) \\ \Psi(a_{i,j,k,z,d}, \gamma) \end{pmatrix} \quad (1)$$

where $\Psi(a, \gamma)$ denotes the application of the second order polynomial function using the coefficients a and input variable γ. The breathing phase d is determined by comparing the current navigator value with its predecessor. Once the 3D motion fields for each of the control points are determined, a denser motion field is computed using a multilevel B-splines interpolation [28]. The variation of the motion fields as a function of the surrogate signal was modelled separately for inspiration and expiration to consider the hysteresis effects. Realistic respiratory cycle variation is captured using high temporal resolution as well as the three respiration modes (i.e. normal, fast and deep breathing) for the formation of the model. Therefore, for a given surrogate value (e.g. diaphragm position in a respiratory signal) and breathing direction (i.e. inspiration or expiration) the model calculates the corresponding motion fields.

C. Respiratory Signal Database

Respiratory signals describing the vertical displacement of the diaphragm as a function of time were obtained from thirty four ammonia (^{13}NH$_3$) cardiac perfusion PET studies of anonymized datasets of freely breathing patients using a data driven method [30], [31]. The motion signal was extracted using a spectral analysis technique on projection space to identify the voxels with intensity change in PET data, a technique originally proposed by Schleyer *et al.* [30]. Each signal was acquired for 3 *min* of 0.1 *s* duration for each time point. Examples of these signals are presented in Fig. 2.

All thirty four patient studies were investigated, by determining the maximum, minimum and mean motion amplitude in order to calibrate the expected motion amplitude range during a 3 *min* PET study. For each of the thirty four patient curves, the diaphragm motion was measured as the difference between the highest and the lowest diaphragm edge locations on the gated, attenuation-uncorrected,
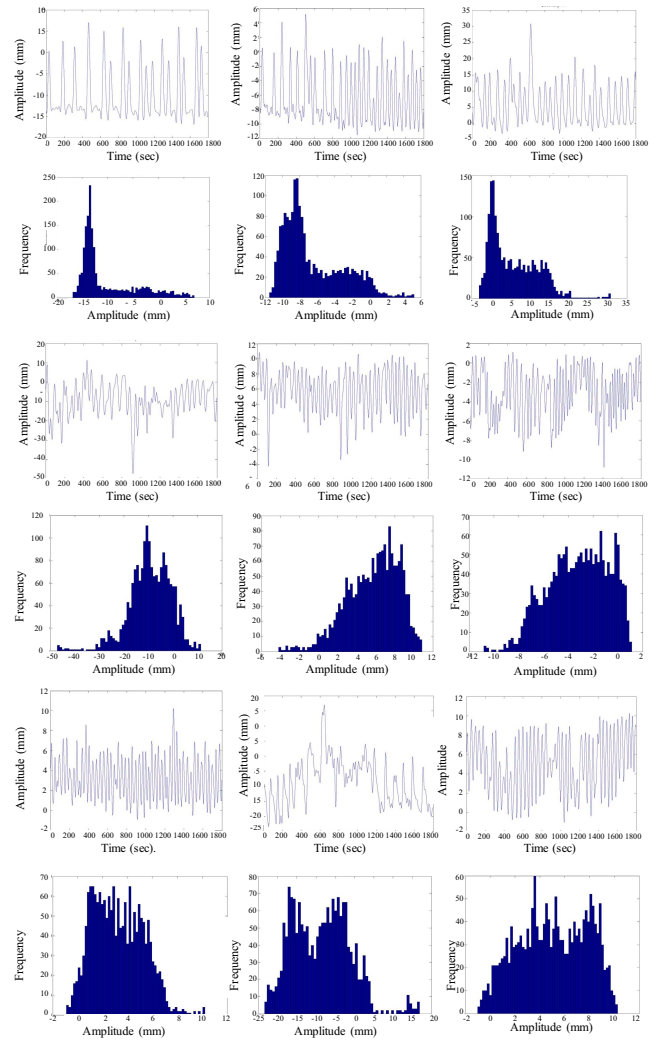

Fig. 2. Examples of breathing curves and corresponding displacement histograms for nine patients.

^{13}NH$_3$ PET images. These attenuation-uncorrected images were used, since they do not suffer from additional attenuation-induced respiratory artifacts. Results indicate that the maximum and the minimum diaphragm motion amplitude, as measured in PET images, were approximately equal to 20 *mm* and 6 *mm*, respectively. This range is consistent with a previous study by Liu *et al.* [32] which reported a maximum displacement 20 *mm* and 15 *mm* and a minimum displacement 5 *mm* and 4 *mm* for the left and right diaphragm, respectively.

The study by Liu *et al.* [32] showed that the variability of the different respiratory signals can be classified into three breathing patterns based on the corresponding displacement histogram. Each of the thirty four signals in the database of thorax PET studies was allocated to one of these three breathing patterns. The most representative signal for each pattern was subsequently selected to be used in this study. The reader is notified that for visualization purposes of the motion artifacts, the most significant and representative signal for each breathing type was selected rather than an average one, as the latter would have created less apparent motion artifacts due to the small size of the corresponding figure.
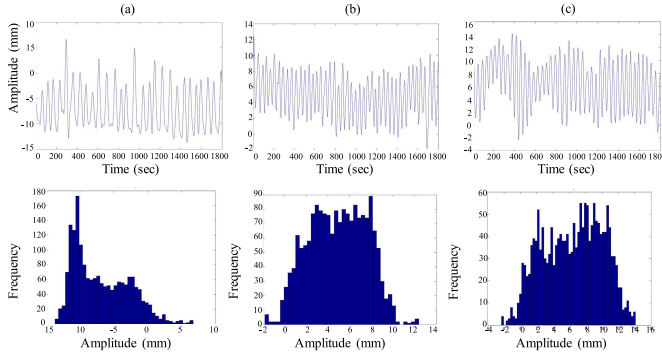
Fig. 3. Example of breathing curves and their displacement histograms for the three breathing types: (a) long quiescent motion periods, (b) regular quiescent motion periods and (c) random baseline shifts [51].

The selected respiratory signals and their displacement histograms are illustrated in Fig. 3. The first signal is characterized by long quiescent motion periods (type-1), the second signal by regular quiescent motion periods (type-2) and the third signal by random baseline shifts (type-3). Note, that for longer acquisition protocols e.g. 60 *min*, the patient respiratory cycle may follow more variable respiration pattern.

With the use of the selected breathing patterns a database with variable diaphragm motion was created based on the above measurements of expected amplitude range in a 3 *min* acquisition. To do this, all signals were firstly shifted to zero median displacement and then scaled to diaphragm amplitudes ranged from 14 to 20 *mm* with a step of 3 *mm* creating a complete database of all three breathing types.

D. ^{18}F-FDG and ^{68}Ga-PSMA 3D Computational Phantoms

One anthropomorphic numerical phantom of the thorax was produced for each tracer, ^{18}F-FDG and ^{68}Ga-PSMA, simulating normal activity distributions. As proposed by Tsoumpas *et al.* [20] a 3D MRI reference image was segmented into different tissue types using intensity thresholds to extract each region of interest (i.e. air, soft tissue, bone and lung tissue). Then, uniform standardized uptake values (SUVs) as typically measured in a clinical acquisition were assigned to each type according to the radiotracer.

For the ^{18}F-FDG distribution, SUVs were assigned to each type as following [33]: 0 for air, 1 for soft tissue, 3.2 for myocardium, 2.5 for liver, 2.3 for bone and 0.5 for lung tissue. Then, synthetic spherical tumors were created and embedded at different locations in the lungs and liver with various characteristics (i.e. size ranging from 6 to 12 *mm* diameter with a step of 2 *mm* and tumor to background ratio ranging from 3:1 to 6:1 with a step of 1). For each combination of size and tumor to background ratio, a synthetic phantom was created with tumors added to identical positions.

For the ^{68}Ga-PSMA distribution, SUVs were assigned to each type of tissue as following [34]–[36]: 0 for air, 1 for soft tissue, myocardium and bone, 5 for liver , and 0.5 for lung tissue. Spherical tumors were also created and embedded in the image at different locations in the lungs and liver with various

TABLE I
KERNEL FWHM AND FWTM FOR X AND Z AXIS (mm)

	FWHM x axis	FWTM x axis	FWHM z axis	FWTM z axis
Cortical bone	2.4	4.3	2.4	4.4
Water	2.6	4.7	2.7	4.8
Lung	2.6	4.8	3.4	6.2

characteristics (i.e. size ranging from 10-12 *mm* diameter with a step of 2 *mm* and tumor to background ratio 3:1).

The effect of positron range was included in the ^{68}Ga-PSMA simulations as the average kinetic energy of the positrons emitted from ^{68}Ga nuclei is much higher than those emitted from the ^{18}F nuclei. Additionally, ^{68}Ga positron range is considerably higher in different materials, in comparison with ^{18}F. Specifically, the lung mean positron range in lung increases by 6.17 *mm* compared to water for ^{68}Ga. For ^{18}F, the difference is 1.28 *mm* [37]. In addition, the existence of a strong magnetic field makes the positron range considerably anisotropic [38]–[40]. For these reasons, a positron range kernel, derived from Monte Carlo simulations was applied to the ^{68}Ga-PSMA numerical phantom prior to the analytical simulations. Note that for ^{18}F the positron range is negligible for the typical clinical scanners resolution, and as such it was not simulated in the current study [40].

To derive the positron range kernel the established Monte Carlo stimulation package, GATE, was utilized. A point source of ^{68}Ga was placed in the center of a phantom, and 10^6 positron annihilations were simulated with the presence of a 3 *T* magnetic field perpendicular to the inferior-superior direction (z axis). We chose water, lung and cortical bone as the representing materials. The simulated cortical bone and lung are given by the ICRU-44 report. Cortical bone was simulated with of 1.68 *gr/cm*^{3} and attenuation coefficient at 511 *keV* equal to 0.15 *cm*$^{-1}$ and lung was simulated with density of 0.26 *gr/cm*^{3} which corresponds to attenuation coefficient 0.0248 *cm*$^{-1}$ at 511 *keV*. Following the simulation, all positron annihilation positions were obtained.

Each voxel may accommodate a large amount of point sources and as such the positron range kernel needs to be adjusted for accuracy. To estimate the density of the kernel for each voxel a variation of the sample distribution function was applied as described by the following equation:

$$DE(x, y, z) = \frac{1}{n} \sum_{i=0}^{R_i/\theta} \sum_{j=0}^{R_j/\theta} \sum_{k=0}^{R_k/\theta} K(x + (i \times \theta),$$
$$y + (j \times \theta), z + (k \times \theta)) \quad (2)$$

where R_i, R_j and R_k denotes the size of each voxel size ($2 \times 2 \times 2$ *mm*^{3}), θ is the sampling rate within the sub-voxel area (0.1 *mm*) n is the total number of repetitions of this cycle, depended by the sampling rate and K is the positron range kernel with resolution similar to the sampling rate, θ [41]. Coronal planes of the kernels for the three tissue types (i.e. cortical bone, water and lung) are presented in Fig. 4. For these kernels, full width at half maximum (FWHM) and full width at tenth maximum (FWTM) are provided in Table 1 for the x axis perpendicular to the magnetic field and z axis, parallel with the magnetic field.
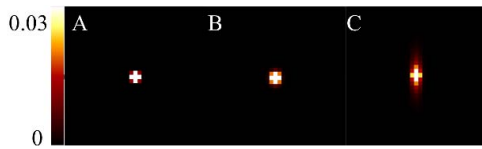
Fig. 4. Coronal planes of the kernels relative to ^{68}Ga in the (A) cortical bone, (B) water and (C) lung tissue at 3 *T*.
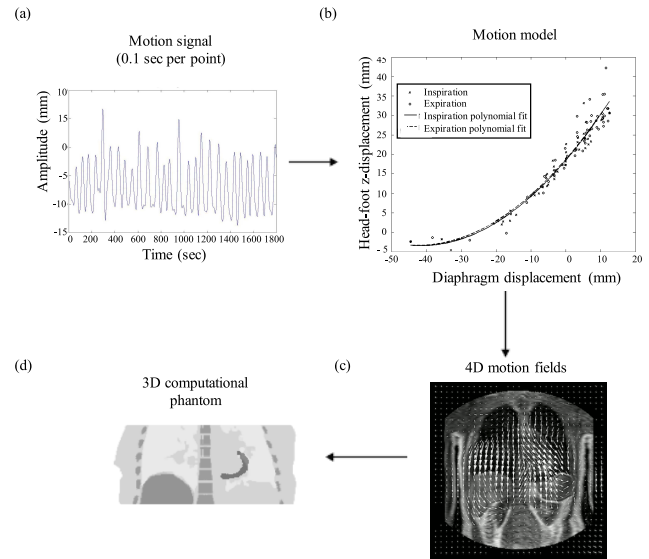

Fig. 5. The 4D simulation is based on a motion model that describes the 3D trajectory (b), of each point in a grid covering the torso (c), as a function of the displacement of the diaphragm (a). The 4D description of the motion in the torso is then used to create the 4D computational phantom (d).

As a next step, a convolution of the radioactivity distribution kernels of each tissue was separately performed, according to the tissue density. The soft tissue, liver and heart were classified as water and the rest (lung, bone) to their corresponding groups. The first step is to apply the distribution function as described by literature [40] and convolve the kernel with the activity distribution for each organ individually and with the proper kernel for it. An important side effect of long positron range is the overlap between regions, most notably in the lung, where the positrons from high emitting areas travel into a less dense medium. To account for this, the borders of the media was considered. The first step is to apply the distribution function as described by literature and convolve the kernel with the activity distribution for each organ individually and with the most appropriate kernel. Afterwards, we detect the voxel adjacent to a new material, where the kernels change. When a kernel crosses to a new material we recalculate the kernel from the border locations and we use the local intensity. Afterwards, the new kernels are applied only to areas containing the adjacent material. Each region of the phantom was treated individually but also in correlation with the neighboring regions for the calculation of kernel variations.

E. Motion Model Application: ^{18}F-FDG and ^{68}Ga-PSMA 4D Computational Phantoms

Respiratory motion was incorporated in the numerical phantoms by applying the deformation fields. These fields were estimated from the dynamic MRI images together and the motion model.

For each respiratory signal, the motion model is used to calculate motion fields necessary to transform the reference distribution (i.e. the 3D tracer uptake distribution) to the relevant respiratory positions and generate the moving phantom. Note that no tracer kinetics within the body or radioactivity physical decay was simulated in this investigation.

The activity distribution was warped using transformations calculated from the motion model for each sampling point of a 3 *min* acquisition signal with 0.1 *s* duration for each point (i.e. 1800 sampling points) as illustrated in Fig. 5. Similarly, the motion fields were applied to the anatomical attenuation maps to create datasets with motion.

For each PET dataset with motion, the projection data can either be simulated without gating or alternatively they can be gated based on amplitude and/or phase of the respiratory signal to generate eight partitions (i.e. gates) over the full respiratory motion cycle [42]. For example, in the case of amplitude-based gating for a given breathing type and amount of motion, the amplitude range can be firstly subdivided into eight equal amplitude bins (i.e. gates) such that each of the

1800 images can be averaged into each corresponding gate creating a respiratory-gated 4D phantom. Therefore, each gate of this phantom includes intra-gate motion and since the PET acquisition system model is in reasonable approximation linear, averaging the radioactivity distributions prior to simulating the projection data will provide similar result as simulating continuous projection data and gating afterwards.

F. Attenuation Maps

Similarly to the procedure described in section II.D, an anatomical 511 *keV* attenuation map was generated by assigning appropriate attenuation values in the segmented regions of the high resolution MRI image. Attenuation values were assigned as following: 0 cm^{-1} for air, 0.096 cm^{-1} for soft tissue, 0.15 cm^{-1} for bone and 0.028 cm^{-1} for lung tissue. The motion model for a respiratory signal was then applied and attenuation images for each of the eight respiratory positions have been created with the same procedure described above for the activity distributions. In this way, a 4D attenuation map was constructed with the attenuation values remaining fixed for each tissue type along the eight gated images, regardless the respiratory position and the existence of motion. This is an approximation that most studies in the literature have adopted [6]. However, as observed by Holman *et al.* [6] changes arise from the density variations in the lung as a result of motion. To enhance the realism of the simulations, the attenuation maps have been processed to include changes in lung attenuation values at different respiratory positions. The lung at expiration has an average HU: -700, which is converted to 0.028 cm^{-1} at 511 *keV* [43]. Therefore, for lung tissue simulations, an attenuation value of 0.028 cm^{-1} was used for the most extreme expiration position of the phantom. However, for any other respiratory position, the total lung

volume was calculated and the appropriate attenuation value was assigned using the inverse proportionality law. In this way, a 4D attenuation map was created with variable attenuation values according to the motion state [43].

G. Analytic Simulations and Reconstructions

Each gate of the 4D generated activity distribution was used as input to an analytic PET-acquisition simulation to generate projection data in the form of sinograms for the Philips Gemini scanner as described in [20]. The projection data accounted for photon attenuation, scatter (approximately 33% of the total counts) but not for random coincidences. Statistical (Poisson) noise was added to the projection data such that the overall counts of the whole dataset corresponding to 30 million unscattered coincidences for ^{18}F-FDG [44] and 10 million unscattered coincidences for ^{68}Ga-PSMA [45] (i.e. 3 *min* 3D PET clinical thorax acquisition). Noise in the gated data was accounted for the duration of each corresponding gate. Each respiratory histogram value shows the duration that the patient spends in the specific breathing position (i.e. how many times the specific amplitude was repeated in a respiratory signal).

Each dataset was reconstructed with and without motion correction using the ordered subsets expectation maximization (OSEM) algorithm. All iterative reconstructions were performed with 23 subsets and for a low number of iterations (i.e. 2) as typically used in the clinic. Each slice consisted of 250×250 pixels with size 2×2 mm^2 each, and the entire volume consisted of 87 slices with 2 *mm* thickness. Attenuation and scatter corrections were applied. A motion compensated image reconstruction method (MCIR) was used to obtain the motion corrected images by incorporating the motion information within the reconstruction via the forward and backward warping transformation operators, as described in [46].

III. RESULTS

A. ^{18}F-FDG and ^{68}Ga-PSMA Computational Phantoms

Realistic simulated numerical phantoms with variable diaphragm motion amplitude and breathing patterns were created. Figs. 6-7 show examples of slices through the images of the simulated radioactivity distribution for the ^{18}F-FDG and ^{68}Ga-PSMA, respectively. In addition, Figs. 6-7 illustrate the effect of motion in PET acquisitions: the average of the simulated radioactivity distribution for 1800 respiratory positions as created with the use of the motion model combined with a respiratory signal of 3 *min* of 0.1 *s* duration for each time point. The selected respiratory signals for the three breathing types are illustrated for the 20 *mm* maximum motion amplitude. The tumors are blurred out by the effect of motion. Tumors in images representing breathing type-2 and type-3 are affected more by motion than those tumors in images representing breathing type-1.

Fig. 8 illustrates the effect of positron range for ^{68}Ga-PSMA: simulated radioactivity distribution, with and without the presence of kernel convolution. The synthetic tumors were blurred out by the effect of the positron range
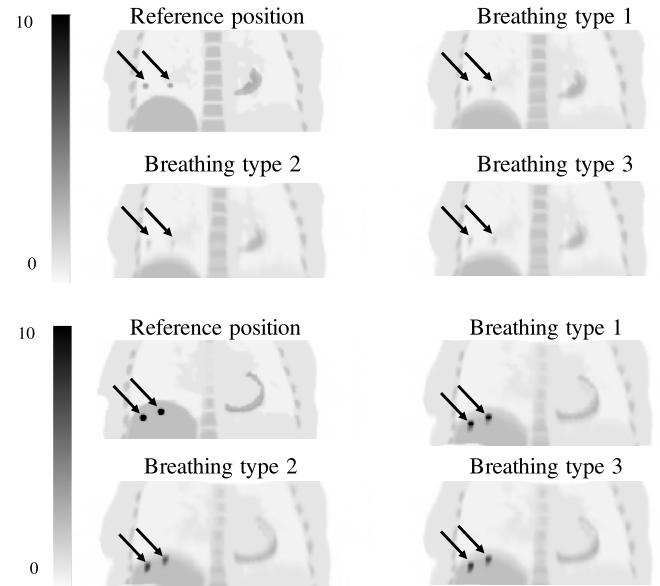

Fig. 6. Examples of coronal planes of the ^{18}F-FDG distribution for one respiratory position and for the average of 1800 respiratory positions showing the motion artifacts. Arrows indicate the tumors. All three breathing types are presented.

Fig. 7. Examples of coronal planes of the ^{68}Ga-PSMA distribution for one respiratory position and for the average of 1800 respiratory positions showing the motion artifacts. Arrows indicate the tumors. All three breathing types are presented.
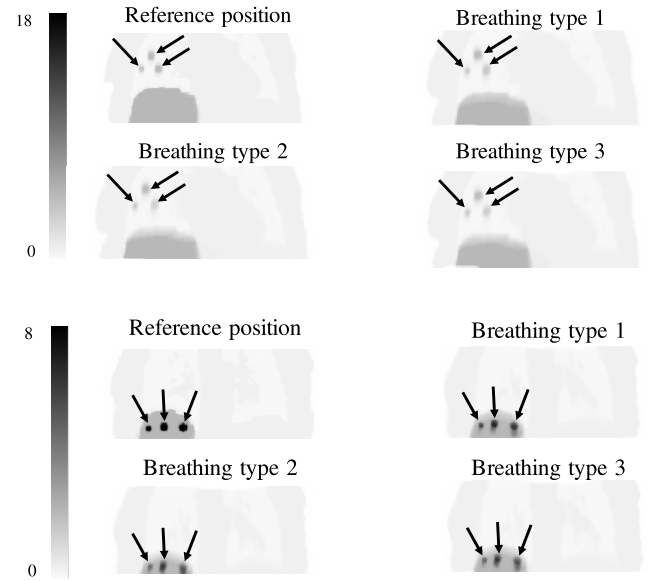
influenced by the presence of the 3 *T* magnetic field. Table 2 lists the characteristics of the tumors and the maximum, mean and standard deviation of the SUV before and after blurring. The values were derived by a segmented tumor using a threshold of 34% to SUVmax. The values represent the underestimation of uptake value and the overestimation of tumor volume that may be caused by the effect of the positron range.

B. Demonstration of Data Reconstruction

Fig. 9 shows example of reconstructed ^{18}F-FDG images, of two different scenarios: all single positions were averaged and reconstructed without and with motion correction using

TABLE II
SYNTHETIC TUMOR CHARACTERISTICS BEFORE AND AFTER APPLYING BLURRING FOR ^{68}GA-PSMA

	Tumor 1 $\varnothing$ 16 *mm* Liver	Tumor 2 $\varnothing$ 16 *mm* Lung	Tumor 3 $\varnothing$ 16 *mm* Lung	Tumor 4 $\varnothing$ 16 *mm* Liver	Tumor 5 $\varnothing$ 16 *mm* Lung	Tumor 6 $\varnothing$ 16 *mm* Lung	Tumor 7 $\varnothing$ 10 *mm* Liver	Tumor 8 $\varnothing$ 10 *mm* Lung	Tumor 9 $\varnothing$ 10 *mn* Lung
Ideal SUV$_{max}$	20	6	6	20	6	6	20	6	6
Blurred SUV$_{max}$	19.99	4.83	4.83	19.99	4.98	4.83	19.77	4.14	4.12
Mean/std SUV	16.34/2.88	3.30/0.94	3.3/0.94	16.23/2.85	3.32/0.93	3.3//0.93	15.07/2.81	2.72/0.80	2.61/0.8(
Theoretical Volume (cm^3)	2.1	2.1	2.1	2.1	2.1	2.1	0.5	0.5	0.5
Measured volume with 34% SUV$_{max}$ threshold (cm^3)	2.2	2.5	2.5	2.0	2.5	2.5	0.9	1.2	1.0

Fig. 8. Simulated radioactivity distribution for the ^{68}Ga-PSMA (a) without blurring and (b) with blurring for ^{68}Ga at 3 T.
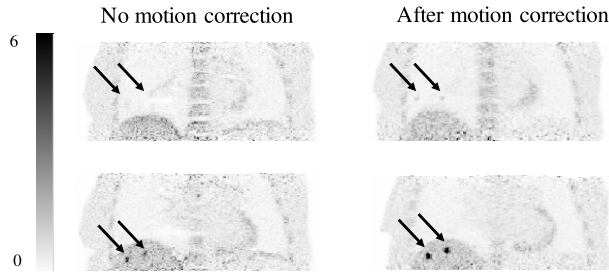

Fig. 9. Example of two selected coronal planes of reconstructed images for ^{18}FFDG distribution with and without motion correction. Arrows indicate the tumors. Results for the breathing type-3 are presented.

MCIR. The impact of motion correction is illustrated for breathing type-3 which is the case mostly affected by motion artifacts. Tumors can be visually observed in the images after motion correction, whilst hardly seen in the images with motion.

IV. DISCUSSION

This paper presents a methodology that can be followed to create realistic PET datasets with aperiodic and even continuous motion, based on a sequence of real MRI acquisitions and a combination of segmentations and image registrations. Although there are various methodologies for producing PET radioactivity distributions with motion, most of them only model a single respiratory cycle, whilst in reality the breathing cycle is not periodic and has cycle-to-cycle variations in magnitude as well as longer inter-cycle variations in both magnitude and period [47], [48], particularly in long PET acquisitions. In this work, PET datasets are produced by incorporating motion modelling based on real representative respiratory signals of three breathing patterns, in line with observations during actual PET acquisitions. Thus, a 4D phantom is created using estimated motion information and

transformation of a 3D tracer uptake distribution to any respiratory position as dictated by the signal (Figs 6-7).

The motion model has the advantage of being able to simulate realistic motion data at any respiratory position, as observed in real human subjects during image sessions. Considering that in real studies respiratory motion is only in part periodic, the method presented in this manuscript enables the realistic simulation of motion trajectories, according to the amplitude and frequency of motion. The model is applicable to any respiratory signal (i.e. different time frames or pattern) by simply replacing the signal used for this study and following the predescribed procedure. Therefore, this investigation can be extended to longer PET acquisitions, e.g. 60-90 *min,* and can integrate further different types of motion. In addition, this method allows simulations of temporal resolution similar to the PET imaging system. In this paper, a subject-specific motion model was used. The proposed simulation scheme could be further extended by the use of a global population-based motion model to provide motion information without the need for patient specific MRI acquisitions [49].

In the example of motion model in Fig. 1, the plot represents the displacements for a specific control point in the image as a function of the head-foot diaphragm translation signal. Although the plot for the specific control point shows an almost identical relationship between inspiration and expiration, this is only an example and it is not the case for all control points in the image. In the motion model used in this paper, the motion fields variation as a function of the surrogate are modelled separately for inspiration and expiration.

In the current study, eight respiratory gates have been used, which are common in clinical practice. Based on literature, six to eight respiratory gates are sufficient, but the optimal number of gates is related with the scanner resolution and motion amplitude [50], which is beyond the scope of the current study. Nevertheless, the proposed methodology can be applied to higher number of gates, though it has to be noted that as the number of gates increases, the process becomes even more computationally demanding.

The substantial travel of the high energy positron emitted by ^{68}Ga results in underestimation of the uptake values and

overestimation of volume as shown in the quantitative analysis presented in Table 2 [38]. Fig. 8 highlights the positron range importance when simulating ^{68}Ga radioactivity distribution. Most blurring is observed in the lungs, where electrons are sparser, causing positrons annihilation distance to increase. For example the corresponding SUV_{max} for the tumor in the lung was 6 before blurring and decreased to 4.13 after blurring. The overestimation of the tumor volume was 71% for a 10 *mm* diameter liver tumor and 123% for a 10 *mm* diameter lung tumor. As a consequence, small metastatic cancerous tumors may be missed. For the ^{68}Ga datasets, both motion and positron range, in strong magnet, are anisotropic effects with their largest impact along the same direction, causing blurring in the images and significantly limiting the PET performance. In a previous study [51], for the clinical tracer ^{18}F-FDG, we have shown that the benefit of increasing the scanner resolution is small for imaging the torso, unless motion correction is applied. However, for the clinical tracer ^{68}Ga-PSMA, even if respiratory motion is successfully corrected, the benefit from the potential improved spatial resolution of future PET scanners will be limited due to the positron range. Therefore, proper correction of the positron range effect should be included in future reconstruction algorithms [52].

Our methodology and the synthetic datasets can provide a useful tool to evaluate the accuracy of motion correction methods [51]–[53] as shown in Fig. 9. The realistically simulated datasets can provide a comprehensive tool for pioneering more accurate and precise management of variable types of motion, including bulk motion [53], which are expected to be necessary particularly in relatively long acquisition protocols.

One limitation of the current datasets is the lack of anatomical detail in the lungs which may not provide sufficiently realistic information of the motion vectors. Methods how to retrieve information from the lungs need to be considered in future dataset generation by utilizing high resolution MRI acquisitions capable to include sufficient signal even in the region of the lungs [55]. Another issue is the limited temporal resolution of the MRI images. The current dynamic images could not be acquired with time window faster than a 700 *ms*, which contributes to an inherent loss of accuracy in the estimation of motion, particularly for the generation of 100 *ms* frames. An additional issue to consider in the future, is the use of human atlases for simulation of bone structures [56] since the UTE sequences require long acquisition times and consequently are subject to motion artifacts, as well [57], [58].

As illustrated, the proposed methodology can be extended to synthesize a large number of PET datasets with realistic motion for several types of patient protocols, radiotracers, number of patients and diseases. An extension of this concept can integrate other types of motion (e.g. cardiac beating [59], [60]) for event by event motion correction [61] of continuously moving humans or even animals [62], which is another active research area.

V. Conclusion

We presented a scheme to simulate realistic synthetic (i.e. 100 *ms*) PET data of two different radiotracers using a combination of dynamic and static MRI acquisitions of healthy volunteers. This approach allows incorporation of models of respiratory motion to generate temporally and spatially correlated MRI and PET datasets, as expected in simultaneous PET-MRI acquisitions. Simulations with realistic anatomy and motion trajectories as those observed in human subjects can help investigate the performance of different reconstruction and motion correction methods. The synthetic images, the corresponding PET datasets will become accessible to the scientific community under the collaborative computational project on synergistic PET-MRI reconstruction: http://www.ccppetmr.ac.uk and / or STIR. The main framework to simulate the data utilized the open source STIR library.

References

[1] J. B. Moody, V. L. Murthy, B. C. Lee, J. R. Corbett, and E. P. Ficaro, "Variance estimation for myocardial blood flow by dynamic PET," *IEEE Trans. Med. Imag.*, vol. 34, no. 11, pp. 2343–2353, Nov. 2015.

[2] W. Siman, O. R. Mawlawi, J. K. Mikell, F. Mourtada, and S. C. Kappadath, "Effects of image noise, respiratory motion, and motion compensation on 3D activity quantification in count-limited PET images," *Phys. Med. Biol.*, vol. 62, no. 2, p. 448, 2016.

[3] A. Bousse *et al.*, "Maximum-likelihood joint image reconstruction/motion estimation in attenuation-corrected respiratory gated PET/CT using a single attenuation map," *IEEE Trans. Med. Imag.*, vol. 35, no. 1, pp. 217–228, Jan. 2016.

[4] A. Turco *et al.*, "Impact of CT-based attenuation correction on the registration between dual-gated cardiac PET and high-resolution CT," *IEEE Trans. Nucl. Sci.*, vol. 63, no. 1, pp. 180–192, Feb. 2016.

[5] G. S. P. Mok, T. Sun, T.-C. Huang, and M. I. Vai, "Interpolated average CT for attenuation correction in PET—A simulation study," *IEEE Trans. Biomed. Eng.*, vol. 60, no. 7, pp. 1927–1934, Jul. 2013.

[6] B. F. Holman, V. Cuplov, B. F. Hutton, A. M. Groves, and K. Thielemans, "The effect of respiratory induced density variations on non-TOF PET quantitation in the lung," *Phys. Med. Biol.*, vol. 61, no. 8, p. 3148, 2016.

[7] T. Küstner *et al.*, "MR-based respiratory and cardiac motion correction for PET imaging," *Med. Imag. Anal.*, vol. 42, pp. 129–144, Dec. 2017.

[8] R. Manber *et al.*, "Practical PET respiratory motion correction in clinical PET/MR," *J. Nucl. Med.*, vol. 56, no. 6, pp. 890–896, 2015.

[9] G. Cruz, D. Atkinson, C. Buerger, T. Schaeffter, and C. Prieto, "Accelerated motion corrected three-dimensional abdominal MRI using total variation regularized SENSE reconstruction," *Magn. Reson. Med.*, vol. 75, no. 4, pp. 1484–1498, 2016.

[10] C. M. Rank *et al.*, "Respiratory motion compensation for simultaneous PET/MR based on highly undersampled MR data," *Med. Phys.*, vol. 43, no. 12, pp. 6234–6245, 2016.

[11] T. Küstner *et al.*, "Self-navigated 4D Cartesian imaging of periodic motion in the body trunk using partial k-space compressed sensing," *Magn. Reson. Med.*, vol. 78, no. 2, pp. 632–644, 2017.

[12] S. J. McQuaid, T. Lambrou, V. J. Cunningham, V. Bettinardi, M. C. Gilardi, and B. F. Hutton, "The application of a statistical shape model to diaphragm tracking in respiratory-gated cardiac PET images," *Proc. IEEE*, vol. 97, no. 12, pp. 2039–2052, Dec. 2009.

[13] H. Zaidi and B. M. W. Tsui, "Review of computational anthropomorphic anatomical and physiological models," *Proc. IEEE*, vol. 97, no. 12, pp. 1938–1953, Dec. 2009.

[14] H. Fayad *et al.*, "The use of a generalized reconstruction by inversion of coupled systems (GRICS) approach for generic respiratory motion correction in PET/MR imaging," *Phys. Med. Biol.*, vol. 60, no. 6, p. 2529, 2015.

[15] M.-P. Garcia et al., "OSSI-PET: Open-access database of simulated [^{11}C] raclopride scans for the inveon preclinical PET scanner: Application to the optimization of reconstruction methods for dynamic studies," IEEE Trans. Med. Imag., vol. 35, no. 7, pp. 1696–1706, Jul. 2016.

[16] A. Le Maitre et al., "Incorporating patient-specific variability in the simulation of realistic whole-body ^{18}F-FDG distributions for oncology applications," Proc. IEEE, vol. 97, no. 12, pp. 2026–2038, Dec. 2009.

[17] W. P. Segars and B. M. W. Tsui, "MCAT to XCAT: The evolution of 4-D computerized phantoms for imaging research," Proc. IEEE, vol. 97, no. 12, pp. 1954–1968, Dec. 2009.

[18] H. Zaidi and X. G. Xu, "Computational anthropomorphic models of the human anatomy: The path to realistic Monte Carlo modeling in radiological sciences," Ann. Rev. Biomed. Eng., vol. 9, pp. 471–500, Aug. 2007.

[19] C. Tsoumpas and A. Gaitanis, "Modeling and simulation of 4D PET-CT and PET-MR images," PET Clin., vol. 8, no. 1, pp. 95–110, 2013.

[20] C. Tsoumpas et al., "Fast generation of 4D PET-MR data from real dynamic MR acquisitions," Phys. Med. Biol., vol. 56, no. 20, pp. 6597–6613, 2011.

[21] S. Jan et al., "GATE: A simulation toolkit for PET and SPECT," Phys. Med. Biol., vol. 49, no. 19, pp. 4543–4561, 2004.

[22] K. Thielemans et al., "STIR: Software for tomographic image reconstruction release 2," Phys. Med. Biol., vol. 57, no. 4, pp. 867–883, 2012.

[23] C. Comtat, P. Kinahan, M. Defrise, C. Michel, C. Lartizien, and D. W. Townsend, "Simulating whole-body PET scanning with rapid analytical methods," in Proc. IEEE Nucl. Sci. Symp. Med. Imag. Conf., vol. 3. Oct. 1999, pp. 1260–1264.

[24] T. Merlin. (2016). Customizable and Advanced Software for Tomographic Reconstruction (CASTOR). [Online]. Available: http://www.castor-project.org/

[25] H. Zaidi and M. Becker, "The promise of hybrid PET/MRI: Technical advances and clinical applications," IEEE Signal Process. Mag., vol. 33, no. 3, pp. 67–85, May 2016.

[26] R. Manber et al., "Joint PET-MR respiratory motion models for clinical PET motion correction," Phys. Med. Biol., vol. 61, no. 17, p. 6515, 2016.

[27] C. Buerger et al., "Investigation of MR-based attenuation correction and motion compensation for hybrid PET/MR," IEEE Trans. Nucl. Sci., vol. 59, no. 5, pp. 1967–1976, Oct. 2012.

[28] C. Buerger, T. Schaeffter, and A. P. King, "Hierarchical adaptive local affine registration for fast and robust respiratory motion estimation," Med. Imag. Anal., vol. 15, no. 4, pp. 551–564, 2011.

[29] A. P. King, C. Buerger, C. Tsoumpas, P. K. Marsden, and T. Schaeffter, "Thoracic respiratory motion estimation from MRI using a statistical model and a 2-D image navigator," Med. Imag. Anal., vol. 16, no. 1, pp. 252–264, 2012.

[30] P. J. Schleyer, M. J. O'Doherty, S. F. Barrington, and P. K. Marsden, "Retrospective data-driven respiratory gating for PET/CT," Phys. Med. Biol., vol. 54, no. 7, pp. 1935–1950, 2009.

[31] P. J. Schleyer, M. J. O'Doherty, and P. K. Marsden, "Extension of a data-driven gating technique to 3D, whole body PET studies," Phys. Med. Biol., vol. 56, no. 13, pp. 3953–3965, 2011.

[32] C. Liu, L. A. Pierce, II, A. M. Alessio, and P. E. Kinahan, "The impact of respiratory motion on tumor quantification and delineation in static PET/CT imaging," Phys. Med. Biol., vol. 54, no. 24, pp. 7345–7362, 2009.

[33] S. Kershah et al., "Comparison of standardized uptake values in normal structures between PET/CT and PET/MRI in an oncology patient population," Molecular Imag. Biol., vol. 15, no. 6, pp. 776–785, 2013.

[34] R. Minamimoto et al., "Pilot comparison of ^{68}Ga-RM2 PET and ^{68}Ga-PSMA-11 PET in patients with biochemically recurrent prostate cancer," J. Nucl. Med., vol. 57, no. 4, pp. 557–562, 2016.

[35] A. Afshar-Oromieh et al., "The theranostic PSMA ligand PSMA-617 in the diagnosis of prostate cancer by PET/CT: Biodistribution in humans, radiation dosimetry, and first evaluation of tumor lesions," J. Nucl. Med., vol. 56, no. 11, pp. 1697–1705, 2015.

[36] T. Pyka et al., "^{68}Ga-PSMA-HBED-CC PET for differential diagnosis of suggestive lung lesions in patients with prostate cancer," J. Nucl. Med., vol. 57, no. 3, pp. 367–371, 2016.

[37] J. Cal-González et al., "Positron range estimations with PeneloPET," Phys. Med. Biol., vol. 58, no. 15, p. 5127, 2013.

[38] S.-Y. Huang, D. Savic, J. Yang, U. Shrestha, and Y. Seo, "The effect of magnetic field on positron range and spatial resolution in an integrated whole-body time-of-flight PET/MRI system," in Proc. IEEE Nucl. Sci. Symp. Med. Imag. Conf., Nov. 2014, pp. 1–4.

[39] G. Soultanidis, N. Karakatsanis, G. Nikiforidis, and G. Loudos, "Study of the effect of magnetic field in positron range using GATE simulation toolkit," J. Phys., Conf. Ser., vol. 317, no. 1, p. 012021, 2011.

[40] O. Bertolli, A. Eleftheriou, M. Cecchetti, N. Camarlinghi, N. Belcari, and C. Tsoumpas, "PET iterative reconstruction incorporating an efficient positron range correction method," Phys. Med., vol. 32, no. 2, pp. 323–330, 2016.

[41] E. Parzen, "On estimation of a probability density function and mode," Ann. Math. Statist., vol. 33, no. 3, pp. 1065–1076, Sep. 1962.

[42] Y. Tsutsui et al., "Accuracy of amplitude-based respiratory gating for PET/CT in irregular respirations," Ann. Nucl. Med., vol. 28, no. 8, pp. 770–779, 2014.

[43] J. A. Zach et al., "Quantitative CT of the lungs and airways in healthy non-smoking adults," Invest. Radiol., vol. 47, no. 10, p. 596. 2012.

[44] R. Boellaard et al., "FDG PET/CT: EANM procedure guidelines for tumour imaging: Version 2.0," Eur. J. Nucl. Med. Molecular Imag., vol. 42, no. 2, pp. 328–354, 2015.

[45] W. P. Fendler et al., "^{68}Ga-PSMA PET/CT: Joint EANM and SNMMI procedure guideline for prostate cancer imaging: Version 1.0," Eur. J. Nucl. Med. Molecular Imag., vol. 44, no. 6, pp. 1014–1024, 2017.

[46] I. Polycarpou, C. Tsoumpas, and P. K. Marsden, "Analysis and comparison of two methods for motion correction in PET imaging," Med. Phys., vol. 39, no. 10, pp. 6474–6483, 2012.

[47] J.-J. Sonke, J. Lebesque, and M. van Herk, "Variability of four-dimensional computed tomography patient models," Int. J. Radiat. Oncol. Biol. Phys., vol. 70, no. 2, pp. 590–598, 2008.

[48] M. V. Siebenthal, G. Székely, U. Gamper, P. Boesiger, A. Lomax, and P. Cattin, "4D MR imaging of respiratory organ motion and its variability," Phys. Med. Biol., vol. 52, no. 6, pp. 1547–1564, 2007.

[49] H. J. Fayad, C. Buerger, C. Tsoumpas, C. Cheze-Le-Rest, and D. Visvikis, "A generic respiratory motion model based on 4D MRI imaging and 2D image navigators," in Proc. IEEE Nucl. Sci. Symp. Med. Imag. Conf., Oct. 2012, pp. 4058–4061.

[50] M. Dawood et al., "Optimal number of respiratory gates in positron emission tomography: A cardiac patient study," Med. Phys., vol. 36, no. 5, pp. 1775–1784, 2009.

[51] I. Polycarpou, C. Tsoumpas, A. P. King, and P. K. Marsden, "Impact of respiratory motion correction and spatial resolution on lesion detection in PET: A simulation study based on real MR dynamic data," Phys. Med. Biol., vol. 59, no. 3, pp. 697–713, 2014.

[52] J. Cal-González, M. Pérez-Liva, J. L. Herraiz, J. J. Vaquero, M. Desco, and J. M. Udías, "Tissue-dependent and spatially-variant positron range correction in 3D PET," IEEE Trans. Med. Imag., vol. 34, no. 11, pp. 2394–2403, Nov. 2015.

[53] T. Shinaji, H. Tashima, E. Yoshida, T. Yamaya, T. Ohnishi, and H. Haneishi, "Time-delay correction method for PET-based tumor tracking," IEEE Trans. Nucl. Sci., vol. 61, no. 6, pp. 3711–3720, Dec. 2014.

[54] C. Kolbitsch, C. Prieto, C. Tsoumpas, and T. Schaeffter, "A 3D MR-acquisition scheme for nonrigid bulk motion correction in simultaneous PET-MR," Med. Phys., vol. 41, no. 8, p. 082304, 2014.

[55] J. Xu and B. M. W. Tsui, "Improved intrinsic motion detection using time-of-flight PET," IEEE Trans. Med. Imag., vol. 34, no. 10, pp. 2131–2145, Oct. 2015.

[56] H. Arabi and H. Zaidi, "Comparison of atlas-based techniques for whole-body bone segmentation," Med. Imag. Anal., vol. 36, pp. 98–112, Feb. 2017.

[57] C. F. Baumgartner et al., "High-resolution dynamic MR imaging of the thorax for respiratory motion correction of PET using groupwise manifold alignment," Med. Imag. Anal., vol. 18, no. 7, pp. 939–952, 2014.

[58] E. Y. Chang, J. Du, and C. B. Chung, "UTE imaging in the musculoskeletal system," J. Magn. Res. Imag., vol. 41, no. 4, pp. 870–883, 2015.

[59] Y. Petibon et al., "Impact of motion and partial volume effects correction on PET myocardial perfusion imaging using simultaneous PET-MR," Phys. Med. Biol., vol. 62, no. 2, p. 326, 2016.

[60] T. Feng, J. Wang, G. Fung, and B. Tsui, "Non-rigid dual respiratory and cardiac motion correction methods after, during, and before image reconstruction for 4D cardiac PET," Phys. Med. Biol., vol. 61, no. 1, p. 151, 2015.

[61] C. Chan et al., "Non-rigid event-by-event continuous respiratory motion compensated list-mode reconstruction for PET," IEEE Trans. Med. Imag., no. 99, 2017.

[62] A. Kyme, S. Meikle, C. Baldock, and R. Fulton, "Tracking and characterizing the head motion of unanaesthetized rats in positron emission tomography," J. Roy. Soc. Interface, vol. 9, no. 76, pp. 3094–3107, 2012.